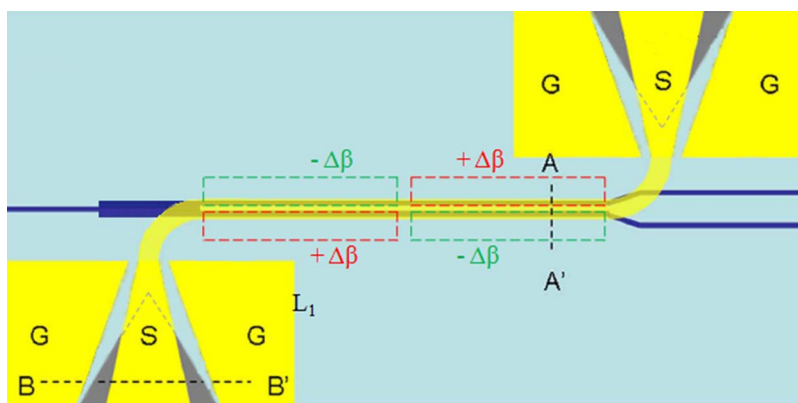# Highly Linear Broadband Optical Modulator Based on Electro-Optic Polymer

Volume 4, Number 6, December 2012

Xingyu Zhang
Beomsuk Lee
Che-yun Lin
Alan X. Wang
Amir Hosseini
Ray T. Chen

Highly Linear Broadband Optical Modulator Based on Electro-Optic Polymer

Xingyu Zhang,[1] **Beomsuk Lee,**[1] **Che-yun Lin,**[1] **Alan X. Wang,**[2] **Amir Hosseini,**[3] **and Ray T. Chen**[1]

[1]The University of Texas at Austin, Austin, TX 78758 USA
[2]Oregon State University, Corvallis, OR 97331 USA
[3]Omega Optics, Inc., Austin, TX 78759 USA

Abstract: In this paper, we present the design, fabrication, and characterization of a traveling-wave directional coupler modulator based on electro-optic polymer, which is able to provide both high linearity and broad bandwidth. The high linearity is realized by introducing $\Delta\beta$-reversal technique in the two-domain directional coupler. A traveling-wave electrode is designed to function with bandwidth–length product of 302 GHz·cm, by achieving low microwave loss, excellent impedance matching, and velocity matching, as well as smooth electric-field profile transformation. The 3-dB bandwidth of the device is measured to be 10 GHz. The spurious-free dynamic range of 110 dB $\pm$ 3 Hz$^{2/3}$ is measured over the modulation frequency range of 2–8 GHz. To the best of our knowledge, such high linearity is first measured at the frequency up to 8 GHz. In addition, a 1 × 2 multimode interference 3-dB splitter, a photobleached refractive index taper, and a quasi-vertical taper are used to reduce the optical insertion loss of the device.

Index Terms: Linear modulator, traveling-wave electrode, electro-optic (EO) polymer, directional coupler, $\Delta\beta$ reversal, spurious-free dynamic range (SFDR).

1. Introduction

Optical modulators in analog optical links are required to have high modulation efficiency, good linearity, and large bandwidth. Existing commercial LiNibO$_3$ Mach–Zehnder (MZ) modulators have intrinsic drawbacks in linearity to provide high-fidelity communication. When multiple tones of signals (f_1 and f_2) are simultaneously carried over a link, nonlinear intermodulation distortion signals are generated. The third-order intermodulation distortions (IMD3s), which are the interactions between fundamental frequencies and harmonics and occur at ($2f_1 - f_2$) and ($2f_2 - f_1$), are considered the most troublesome among all the nonlinear distortions because they usually fall at frequencies very close to fundamental frequencies and are in the pass band of the system. The spurious-free dynamic range (SFDR) is defined as the dynamic range between the smallest signal that can be detected in a system and the largest signal that can be introduced into the system without creating detectable distortions in the bandwidth of concern [1]. The SFDR of high frequency analog optical links is limited by the system noise and the nonlinearity of modulation process. In order to improve the linearity of modulators, various efforts had been taken either electronically [2], [3] or optically [4]–[6] to suppress the IMD3s. A shortcoming common in all these linearization techniques is that the improved linearity is achieved at the expense of sacrificing the simple device design. A bias-free Y-fed directional coupler (YFDC) modulator, on the other hand, had been

proven to possess a highly linear transfer function without loss of the simplicity of device design [7]. Even higher linearity is achievable when YFDC is incorporated with $\Delta\beta$-reversal technique [8], [9]. We previously demonstrated a polymer based two-domain YFDC modulator with the $\Delta\beta$-reversal at low modulation frequencies as a proof of concept [10], where we achieved the SFDR of 119 dB/Hz$^{2/3}$ with 11-dB enhancement over the conventional MZ modulator.

In addition to the requirement of high linearity, the bandwidth is another important factor in evaluating the performance of a modulator. The first demonstration of optical modulation at GHz frequencies was done on a traveling-wave electro-optic (EO) LiNibO$_3$ modulator in the 1970s [11], [12]. A traveling-wave modulator based on an EO polymer operating in the GHz frequency regime was demonstrated in 1992 [13]. Later on, a polymeric modulator operating over 100 GHz was verified by groups at UCLA and USC [14]. Up until today, the highest frequency that the polymer modulator can work at was demonstrated to be as high as 200 GHz by Bell Laboratories [15]. Polymer EO modulators can offer several advantages over the mature LiNibO$_3$ modulators due to the special properties of polymer materials as below [16]–[18]. Excellent velocity matching between microwaves and optical waves can be achieved due to a close match between the refractive index of polymers at microwave and optical frequencies, enabling ultrabroad bandwidth operation. The intrinsic relatively low dielectric constant of polymers (2.5–4) also enables 50-Ω driving electrodes to be easily achieved. Polymers also have very large EO coefficients, γ_{33}, which is advantageous for subvolt half-wave switching voltage (V_π) [19]–[21]. For example, CDL1/PMMA, an EO polymer with $\gamma_{33} = 60$ pm/V, was used to achieve $V_\pi = 0.8$ V [19]. Another EO polymer with a very large $\gamma_{33} = 306$ pm/V was developed through controlled molecular self-assembly and lattice hardening [22]. In comparison, the EO coefficient of LiNibO$_3$ is only about 30 pm/V. In addition, the refractive index of polymers (1.6–1.7) is nearly matched to that of glass optical fibers (1.5–1.6), enabling small Fresnel reflection loss at interfaces in butt-coupling. Polymers can be highly transparent, and the absorption loss can be below 0.1 dB/cm at all key communication wavelengths [17]. And also, polymers are spin-on films so they can be easily spin-coated onto any substrate. Recently, EO modulations on extremely small geometrical footprints have been demonstrated by infiltrating EO polymer into slot waveguides [23] or slotted photonic crystal waveguides [24]. So far, the largest effective in-device $\gamma_{33} = 735$ pm/V and the smallest $V_\pi L = 0.44$ V · mm have been demonstrated by our group using EO polymer infiltrated silicon slotted photonic crystal waveguides [25]. Further-more, compared with the difficult implementation of the domain inversion technique on LiNibO$_3$ [26], $\Delta\beta$-reversal can be easily achieved by domain-inversion poling on EO polymers. Based on the above advantages of polymer materials, EO polymer modulators have shown great potentials for a variety of applications, such as telecommunication, analog-to-digital conversion, phased-array radar, and electrical-to-optical signal transduction. Now, polymer-based modulators with high reliability have been commercially available [27].

In this paper, we demonstrate an EO-polymer-based traveling-wave directional coupler modulator with $\Delta\beta$-reversal to extend the high linearity performance to the GHz frequency regime. A traveling-wave electrode with a unique design for RF microprobe coupling is fabricated with low microwave loss, characteristic impedance matching with 50 Ω, and velocity matching between microwaves and optical waves, as well as smooth electric-field profile transformation. The bandwidth–length product of 302 GHz · cm and the 3-dB bandwidth of 10 GHz are achieved. The SFDR of 110 ± 3 dB/Hz$^{2/3}$ is measured over the modulation frequency of 2–8 GHz. In addition, a 1 × 2 multimode interference (MMI) 3-dB splitter, a photobeached refractive index taper, and a quasi-vertical taper, as well as a smooth silver ground electrode, are used to reduce the optical insertion loss of the device.

2. Design

2.1. Optical Waveguide Design

Fig. 1(a) shows the schematic top view of our traveling-wave MMI-fed directional coupler modulator. The cross section of the optical waveguides consisting of three layers of fluorinated polymers (bottom cladding: UV-15LV; core: AJ-CKL1/APC with $\gamma_{33} = 80$ pm/V; and top cladding: UFC-170A)
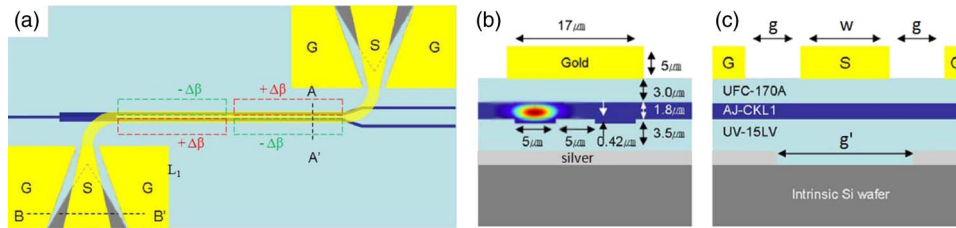
Fig. 1. (a) The schematic top view of the traveling-wave MMI-fed directional coupler modulator with two-domain inversion. The red and green dashed lines indicate the area of EO polymer poled in opposite directions. (b) Cross section corresponding to $A - A'$ in (a), overlaid the optical mode profile in one arm. (c) Cross section corresponding to $B - B'$ in (a). (S: signal electrode, G: ground electrode).

is shown in Fig. 1(b) and (c). Unlike the sine-squared transfer curve of the conventional MZ structure, a proper design of coupling length of directional coupler can provide a linear transfer function [2]–[6]. The linearity of the directional coupler can be further improved by applying $\Delta\beta$-reversal technique to suppress IMD3s [7]–[10]. Multiple-domain inversion, which helps increase the linearity of directional coupler modulator, has been demonstrated by our group [28]. Considering the fabrication and poling complexity, in this paper, we use a two-domain-inversion directional coupler for demonstration. The directional coupler is divided into two domains, where EO polymer in the first domain is poled in the opposite direction with respect to that in the second domain. The push–pull configuration is also applied, in which the two arms of the directional coupler in each domain are poled in opposite directions, to double the EO effect. Finally, a single uniform modulation electric field applied by a traveling-wave electrode can create $\Delta\beta$-reversal, which is indicated by the dashed lines in Fig. 1(a).

The IMD3 suppression of a directional coupler modulator is a sensitive function of the normalized interaction length (S_i), defined as the ratio of the interaction length (L_i) of ith section to the coupling length (l_c). Relative IMD3 suppression of a two-domain directional coupler modulator can be graphically represented by plotting the calculated IMD3 suppressions on (S_1, S_2) plane [29]. $S_1 = S_2 = 2.86$ provides excellent linearity, as well as very high modulation depth [28], and is chosen for demonstration in this paper. For a directional coupler with the total interaction length $(L_1 + L_2)$ of 2 cm, its coupling length for TM mode should be 3496 μm. This coupling length is matched by tuning the parameters of the trench waveguide, such as the core thickness and trench depth, using numerical methods [30]. The thickness of cladding is chosen to be 3.5 μm and 3 μm at the bottom and top, respectively, considering both the requirement of low driving and poling voltage and the prevention of optical absorption by metallic electrodes. The final cross-sectional dimensions are shown in Fig. 1(b). Based on fabrication experiences and actual measurements, the actual bottom width of a 420-nm-deep trench fabricated by reactive ion etching (RIE) is about 4 μm, while the top width is still 5 μm as designed. However, the calculation results show that the resulting coupling length deviation is only 0.55%, which can be explained by the fact that most of the optical power is distributed in the core layer, as shown in Fig. 1(b), and that the field profile interaction happens at the top side of the two trenches, which is unaffected.

A 1×2 MMI 3-dB coupler is designed to equally split the input optical power among two waveguides of a directional coupler, as shown in Fig. 2(a). The symmetric waveguide structure of the MMI-fed directional coupler is intrinsically bias-free, and the modulation is automatically set at 3-dB operation point regardless of the ambient temperature. The dimensions of MMI coupler and the optical power distribution in it are shown in Fig. 2. The total power transmission of this MMI coupler is numerically calculated using eigenmode expansion method [31] to be as high as 94%. This MMI coupler has a large fabrication tolerance and is insensitive to the photolithography resolution. In comparison, as for previously used Y-junction [7], in practice, the fabrication limitations in photolithography and etch resolutions usually lead to a blunt tip under a certain distance between the two waveguides [see Fig. 2(b)] and violate the adiabatic requirement, resulting in extra optical loss [32]. In addition, compared with the previous 1000-μm-long Y-junction [10], the MMI coupler is
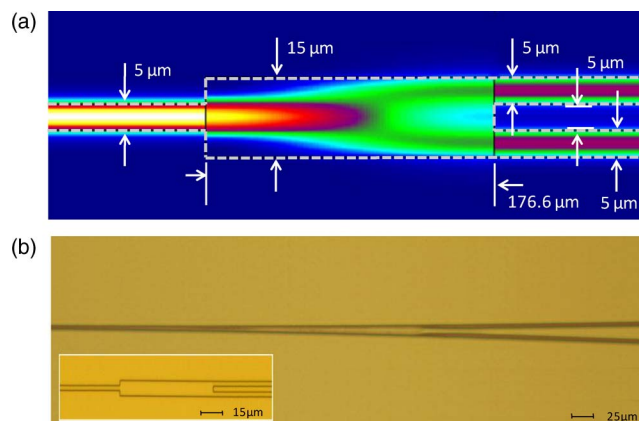
Fig. 2. (a) The top view of a 1 × 2 MMI 3-dB coupler, and the optical power distribution in this MMI coupler. (b) A blunt tip of a fabricated Y-junction due to fabrication limitations, compared to a fabricated MMI coupler shown in the inset.

only 176.6 μm long and is beneficial to decrease the device length. The inset in Fig. 2(b) shows a microscope image of a fabricated MMI coupler compared with a traditionally used Y-junction.

A polymer trench waveguide is designed to support only a single mode. As shown in Fig. 3(a), the TM mode profile of the designed polymer waveguide is calculated using finite-element method [33], with the corresponding optical effective index of 1.599 at 1550 nm. Fig. 3(a) also shows the mode profiles of three single-mode fibers with different mode field diameters (MFD). It can be seen that the mode profile of the polymer waveguide is in an elliptical geometry, with its major axis of about 7 μm and minor axis of about 2.5 μm but that the mode profile of the normally used single-mode fibers (e.g., SM980-5.8-125, Thorlabs) is in a circular geometry with MFD of 10.4 μm. This mode size mismatch can lead to large optical loss in butt-couplings. To reduce such coupling loss, single-mode fibers with MFD of 6.4 μm (e.g., SM1500G80, Thorlabs) or lens fibers with MFD of 2.5 μm (e.g., TSMJ-3U-1550-9/125-0.25-7-2.5-14-2, OZ Optics) can be used as replacements at the input/output (I/O) sides. The power-coupling loss using these three fibers are calculated by considering the overlap integral of mode profiles, as well as Fresnel reflection loss at interfaces [34], [35]. Fig. 3(b) shows the 3-D perspective of the coupling loss as a function of the spatial misalignment in x- and y-directions for these three fibers. To see a clear comparison of these three fibers, a 2-D plot of the same data is shown in Fig. 3(c). It can be seen that the lowest coupling loss, 1.7 dB/facet, can be achieved using lens fibers but that there are very large variations versus misalignment along both x- and y-directions. It can be noticed that, using lens fibers, the coupling efficiency is more sensitive to the misalignment in y-direction than that in x-direction. Using single-mode fibers with MFD of 6.4 μm, a larger alignment tolerance can be achieved, while the peak coupling loss is 2.0 dB/facet, which is just a little higher than that of the lens fibers. Normally used single-mode fibers with MFD of 10.5 μm can provide the lowest misalignment sensitivity but the highest coupling loss, which is up to 4.1 dB/fact. Therefore, considering both coupling loss and misalignment tolerance, a single-mode fiber with MFD of 6.4 μm is finally chosen for our experiment.

Another way to reduce the optical coupling loss due to mode size mismatch is to design a taper structure. Here, refractive index tapers are designed at the passive regions of the waveguides so that the optical mode profile at the I/O ends of the polymer waveguide can better match that of the I/O optical fibers. The working mechanism is shown in Fig. 4(a). Refractive index variation of EO polymer core at the passive regions of the waveguide is created by UV photobleaching method, using a gray-scale photomask or discrete step mask-shifting scheme [36]. This refractive index variation leads to the gradual change of optical mode size along the taper, so that the waveguide modes at the facets are large enough to match that of I/O fibers. In addition, to minimize the severe mode size mismatch in vertical direction that is shown in Fig. 3(a), a quasi-vertical taper structure [37]
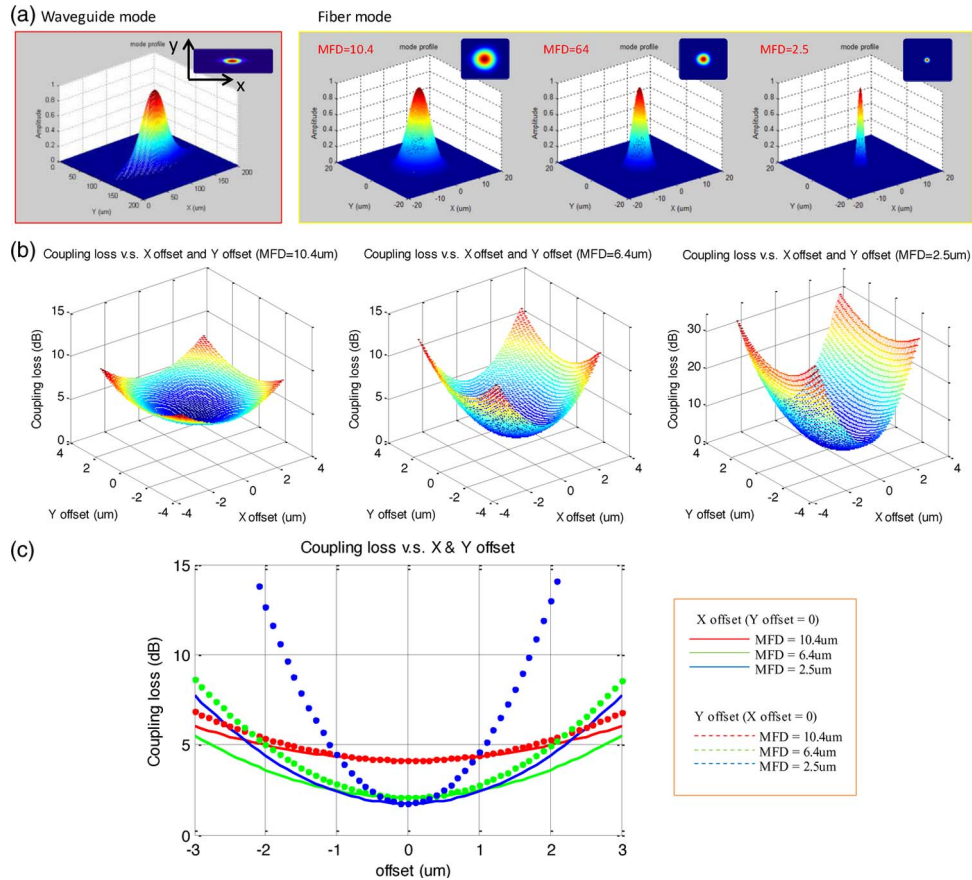
Fig. 3. (a) Optical mode profile in a polymer waveguide, compared with the optical mode profiles in I/O fibers with MFD of 10.4 μm, 6.4 μm and 2.5 μm. (b) The 3-D perspective of the calculated coupling loss versus the misalignment in *x*- and *y*-direction, for using three different I/O fibers. (c) The 2-D plot of the calculated coupling loss versus the misalignment in *y*- and *y*-direction. Red curves, green curves and blue curves represent the coupling loss using a fiber with MFD of 10.4 μm, 6.4 μm and 2.5 μm, respectively, and solid curves and dashed curves represent the coupling loss versus the misalignment in *x*- and *y*-directions, respectively.

is designed as shown in Fig. 4(b). It can be fabricated by standard photolithography and RIE twice. After a trench is etched on the bottom cladding polymer, a V-shape groove is etched again into the trench near the I/O facets. This structure works as an optical mode transformer. Because the trenches are deeper at the facets than in the active regions of waveguide, the waveguide mode size in vertical direction becomes larger at the facets and can better match the I/O fiber mode. Numerical calculations using beam propagation method [38] show that the combination of these two tapers can significantly reduce the optical coupling loss by 3 dB/facet.

Other than the coupling loss, the roughness of polymer waveguide sidewalls usually causes large scattering loss when light propagates in the waveguide. Thus, silver is selected as the ground electrode material, and its smooth surface helps reduce waveguide sidewall roughness originating from the scattering of UV light in photolithography. Compared with other metals, silver is also beneficial to suppress the microwave conductor loss owing to its very low resistivity.

2.2. Traveling-Wave Electrode Design

To extend the highly linear modulation to GHz frequency regime, a traveling-wave electrode is necessary. Some basic requirements for the design of a high-speed traveling-wave electrode are [39]: 1) impedance matching between the microwave guides and external electrical connectors; 2) velocity matching between the microwave and optical signals; and 3) low electrical loss in the
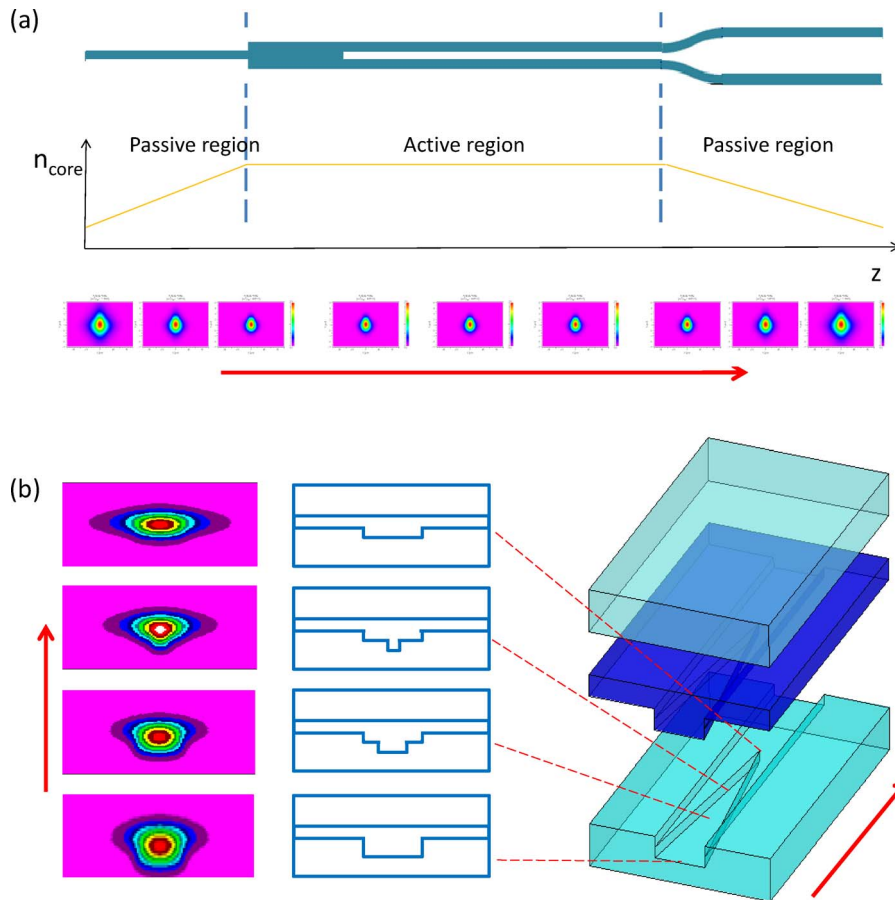
Fig. 4. (a) Refractive index tapers at the passive regions of the MMI-fed directional coupler. The index variation of the photobleached EO polymer in the core layer leads to the gradual change of optical mode size along the taper. (b) A quasi-vertical taper at one facet of polymer waveguide used for mode profile transformation in vertical direction. The red arrows indicate the beam propagation direction.

microwave guides. In addition to the above requirements, when designing a transition between different types of microwave guides, electric-field matching [40], [41] should also be a concern in order to reduce the microwave coupling loss. In our device structure, polymer is considering the alignment of modulation field with the direction of the γ_{33} in the poled EO polymer film, which is in vertical direction in our device configuration; therefore, a microstrip line is a natural choice for the best alignment. Fig. 5(a) shows the schematic cross section of the designed gold microstrip line overlaid the contour of the normalized electric potential calculated by finite-element method [33]. It can be seen that both arms of the directional coupler waveguide are under the effect of a uniform modulation field between the microstrip line and the ground electrode, and hence, the overlap integral between the optical mode and the RF modulation field can be maximized. In quasi-static analysis, the characteristic impedance Z_0 and the microwave effective index n_m of a transmission line can be expressed as [39], [42]

$$Z_0 = \frac{1}{c(CC_a)} \tag{1}$$

$$n_m = \left(\frac{C}{C_a}\right)^{1/2} \tag{2}$$

where C_a is the capacitance per unit length of the electrode structure with the dielectrics replaced by air, C is the capacitance per unit length with the dielectrics present, and c is the speed of light in
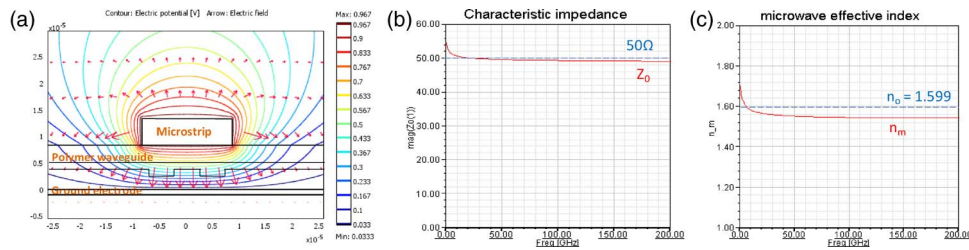
Fig. 5. (a) The schematic cross section of a microstrip line with design parameters overlaid the contour of the normalized electric potential. The red arrows indicate the direction of electric field. (b) The characteristic impedance of the microstrip line over the frequency range 1–200 GHz. The solid red curve indicates the characteristic impedance and the dashed blue line indicates the 50 Ω. (c) The microwave effective index of the microstrip line over the frequency range 1–200 GHz. The solid red curve indicates the microwave effective index and the dashed blue line indicates the optical effective index of 1.599.

vacuum. The frequency-dependent characteristic impedance and microwave effective index can be numerically calculated using finite-element method [43] to match 50 Ω and optical effective index of 1.599, respectively. Conductor loss and dielectric loss are considered in the calculation so that the results are accurate enough and close to the real case. Given the relative dielectric constant $\varepsilon_r = 3.2$, the gap between top and bottom electrodes $h = 8.3$ μm and the microstrip thickness $t = 5$ μm from the waveguide dimensions and the fabrication conditions, the characteristic impedance of 50 Ω can be matched when the microstrip width w = 17 μm. As shown in Fig. 5(b) and (c), over the frequency range of 1–200 GHz, the characteristic impedance varies within 49–54.5 Ω, and the microwave effective index varies within 1.54–1.7. It can be noticed in Fig. 5(b) that the characteristic impedance at low frequencies is relatively higher than that at high frequencies. This is because the internal inductance of the microstrip line decreases with frequency and becomes negligible when skin effect kicks in. Based on fabrication experience and actual measurements, the electroplated gold microstirp line does not have a perfect vertical sidewall but a wall angle of 84°; however, the variation of Z_0 and n_m due to this wall angle are calculated to be within 1 Ω and 0.005, respectively, which can be negligible. The bandwidth–length product due to the velocity mismatch can be calculated as [11], [39], [44], [45]

$$f \cdot L \cong \frac{1.9c}{\pi |n_m - n_o|} \qquad (3)$$

where f is the modulation frequency, L is the interaction length, c is the speed of light in vacuum, n_m is the microwave effective index of the microstrip line, and n_o is the optical effective refractive index of polymer waveguide. Using (3), the bandwidth–length product can be theoretically calculated to be up to 306 GHz · cm, corresponding to a modulation frequency limit of 153 GHz for a 2-cm-long microstrip line.

To couple the RF power from a GSG microprobe [e.g., ACP40-GSG-250, Cascade Microtech; probe tip width: 50 μm; pitch: 500 μm, as shown in Fig. 6(b)] into the 17-μm-wide microstrip line with minimum coupling loss, a 1.1-mm-long quasi-coplanar waveguide (CPW) taper is designed at input end, as shown in Fig. 6(b). The top width and gap of the CPW [w and g in Fig. 6(a)] are gradually changed along the taper to match the dimension of a RF microprobe. In the transition between the CPW and the microstrip line, the electric-field profiles of these two microwave guides should be matched to reduce microwave coupling loss. Therefore, unlike the conventional CPW, the ground electrode under the taper is partially removed, and the bottom gap [g' in Fig. 6(a)] is gradually tuned along the taper based on ground shaping technique [40], [41], so that there is a smooth transformation of electric-field profile in the CPW-to-microstrip transition [33], while 50 Ω is matched at all points along the transition direction [43], as shown in Fig. 6. At the output end, a similar microstrip-to-CPW transition taper is designed to couple the RF power from the microstrip line to another GSG microprobe [see Fig. 1(a)]. What is more, for the design to be valid, the resistivity of silicon substrate
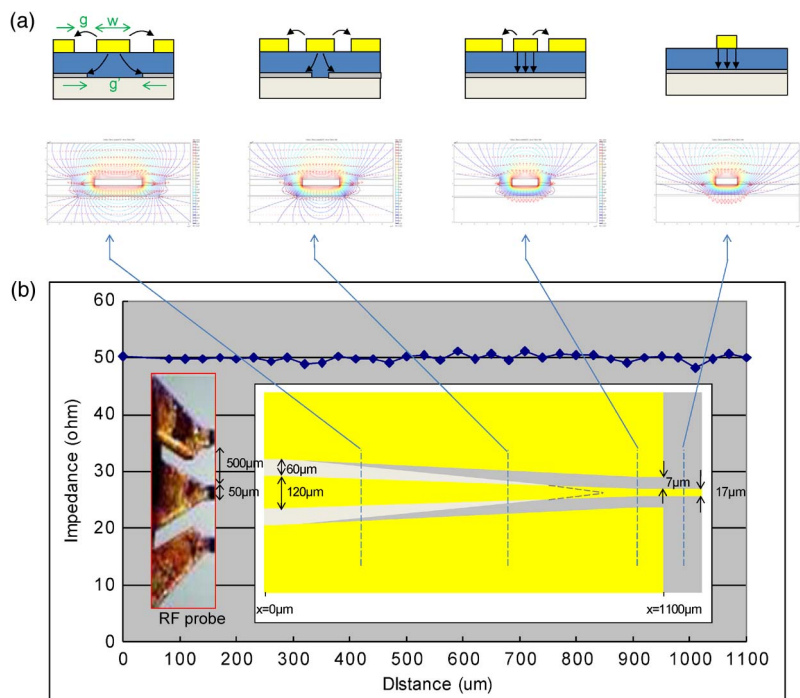
Fig. 6. (a) The schematic of a smooth transformation of electric-field profile in the CPW-to-microstrip transition at the input end of traveling-wave electrode. The corresponding distribution of electric field and electric potential along this transition taper is calculated with finite-element method. (b) The top view of the quasi-CPW taper, matching the size of a microprobe. The characteristic impedance (at 10 GHz) is matched with 50 Ω along the transition direction.

should be sufficiently high (typical l k$\Omega \cdot$ cm or higher). Otherwise, the finite conductivity of silicon substrate allows the formation of microstrip mode between the signal electrode and silicon substrate, and this microstrip mode would become dominant at wide part of the taper and hinder 50-Ω matching. Therefore, an intrinsic silicon wafer with ultrahigh resistivity (6–10 k$\Omega \cdot$ cm) is used as the substrate of our device.

3. Fabrication

Fig. 7 illustrates the fabrication process flow. The device is fabricated on an ultrahigh resistivity silicon wafer. A 1-μm-thick silver film is deposited by electron-beam evaporation and then patterned using liftoff process, to serve as the ground electrode for poling process, as well as for RF transmission. A polymer trench waveguide is fabricated by spin-coating, photolithography, and RIE, in which the EO polymer is formulated by doping 25 wt.% of AJ-CKL1 chromophore into amorphous polycarbonate (APC). 150-nm-thick gold poling electrodes are deposited by electron-beam evaporation and patterned by liftoff process. 300-nm-thick silicon dioxide is deposited by electron-beam evaporation to cover the entire surface of the device as a protection layer. Then, contact windows are opened on the silicon dioxide using photolithography and wet etching method, so that the electrodes can be exposed to the probe needles in the following poling process.

Poling is the most important step throughout the entire process since the EO coefficient of a device is determined by poling efficiency [46], [47]. Among several developed poling techniques [48]–[52], we employ thermally assisted electric-field contact poling [53] in this paper. In the push–pull configuration, two adjacent poling electrodes above the two arms of directional coupler have opposite polarities, and thus, the electric field formed between electrodes is very strong, as shown in Fig. 8(a). Given the electrode separation of 5 μm, the polymer waveguide thickness of 8.3 μm and the poling electric field of typically ±100 V/μm applied vertically across the polymer waveguide, the
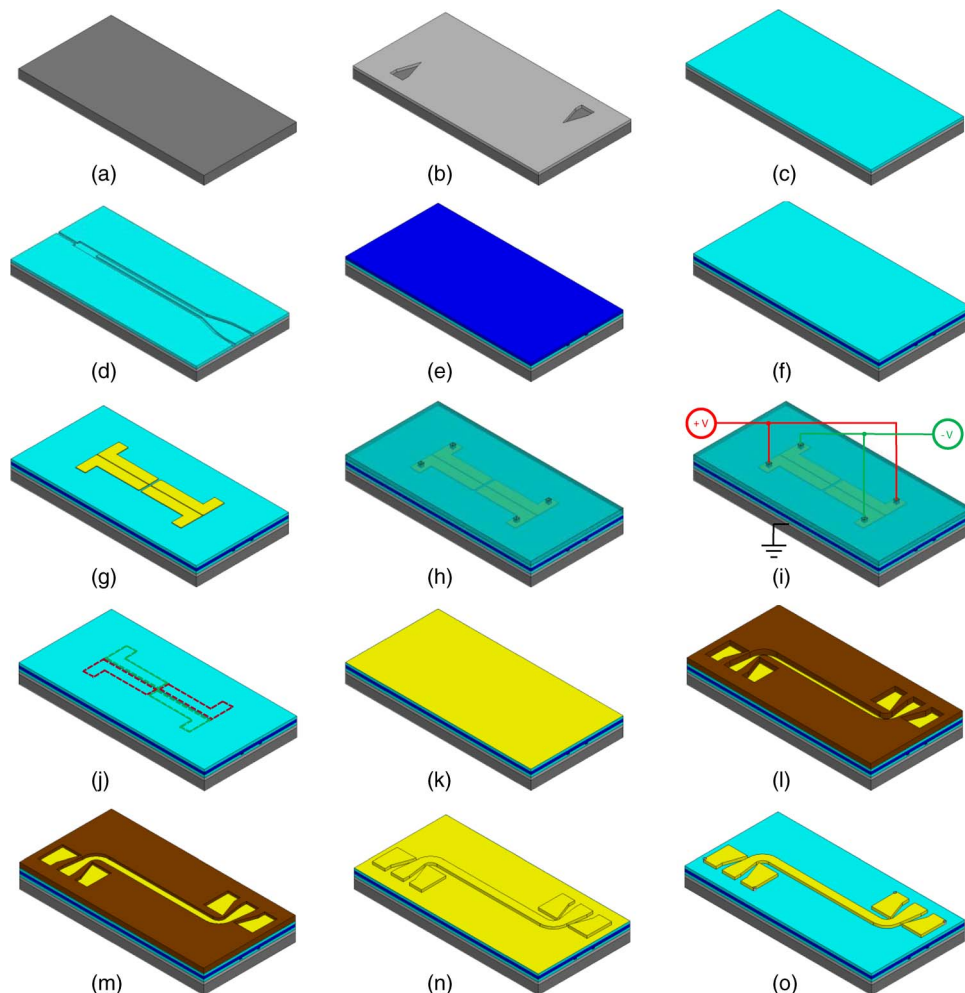
Fig. 7. Fabrication process flow. (a) An ultrahigh resistivity silicon wafer. (b) Ground electrode deposition and patterning. (c) Bottom cladding deposition. (d) Waveguide patterning. (e) EO polymer formulation and deposition. (f) Top cladding deposition. (g) Poling electrode deposition and patterning. (h) Protection layer deposition and patterning. (i) Poling. (j) Removal of protection layer and poling electrode. (k) Seed layer deposition. (l) Buffer mask deposition and patterning. (m) Traveling wave electrode electroplating. (n) Buffer mask removal. (o) Seed layer removal and vias drilling.

maximum electric field between two adjacent electrodes is calculated to be over 300 V/μm [33]. This increases the probability of dielectric breakdown, which can easily damage the device. To prevent this, the deposited thick silicon dioxide serves as a protection layer, as shown in Fig. 8(a), due to its good insolating property and high dielectric strength (up to 1000 V/μm). Experimental tests show that the poling electric field up to 150 V/μm can be applied on our device structure at the glass transition temperature ($T_g = 140$ °C) of EO polymer without dielectric breakdown. This can significantly increase the poling efficiency. In addition, alternating-pulse poling technique [54], [55] is used to further prevent dielectric breakdown. As shown in Fig. 8(b), the positive and negative voltage sources are controlled by dual pulse with π-phase shift from a dual-function generator, so that two opposite polarities are not applied at the same time. Four diodes are used as clampers. Based on testing experience, the frequency of the alternating pulses should be set to be 1–10 Hz to avoid dielectric breakdown. During the poling process, the temperature is controlled to increase from room temperature to T_g and then quickly decrease back to room temperature. Throughout the entire poling process, leakage current is monitored by a picoammeter. A current-limiting resistor and two back-to-back diodes are used in the circuit connection to protect the picoammeter from being
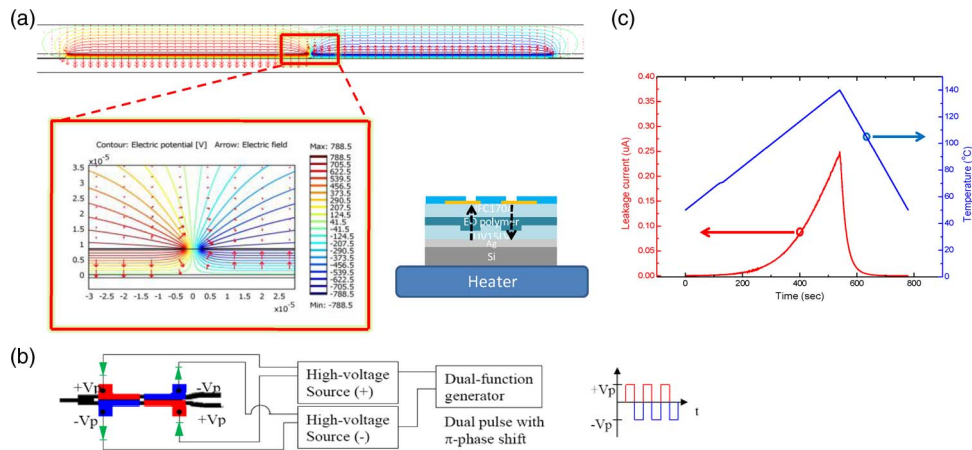
Fig. 8. (a) The cross section of poling electrodes above the polymer waveguide overlaid the electric potential distribution in push–pull poling configuration. (b) The schematic of push–pull, two-domain inversion, alternating-pulse poling. (c) The temperature dependence of leakage current during the poling time.

damaged by any unexpected breakdown-induced high current. Fig. 8(c) shows a leakage current curve depending on the controlled temperature during the poling time.

After poling is done, the silicon dioxide layer and the poling electrodes are removed by wet etching method. A 50-nm-thick gold seed layer with 5-nm-thick chromium adhesion buffer is then deposited above the polymer waveguide by electron-beam evaporation. The buffer mask for the traveling-wave electrode is patterned on 10-μm-thick AZ-9260 photoresist by photolithography. A 5-μm-thick gold film is electroplated using Techni-Gold 25ES electrolyte. A constant current of 8 mA is used in the entire gold electroplating process. For the electroplating area of about 11 cm^2, the corresponding current density is as low as 0.73 mA/cm^2, which enables a uniform gold thickness. The conductivity of the electroplated gold film is measured to be 2.2 $\times$ 10^7 S/m. The coplanar and ground electrodes are then connected with silver epoxy through via holes. Finally, the device is diced, and the waveguide facets are polished.

4. Testing

4.1. Electrode Characterization

The performance of the fabricated traveling-wave electrode is characterized by a vector network analyzer (HP 8510C). Two air coplanar probes (ACP40-GSG-250, Cascade Microtech) are used to couple RF power into and out of the tapered quasi-CPWs. The measured microwave loss of the traveling-wave electrode over the frequency range of 1–26 GHz (upper frequency limited by equipment) is presented on the left side in Fig. 9(a). For reference, the theoretically calculated electrode loss using finite-element method [43] is shown on the right side in Fig. 9(a). It can be seen that the measured transmission loss is proportional to the square root of frequency, implying that the microwave loss is dominated by the conductor loss (skin effect loss) of the electrode [56], [57], which is measured to be 0.65 $\pm$ 0.05 dB/cm/GHz$^{1/2}$. The 3-dB electrical bandwidth measured from transmission-loss curve is 10 GHz, nearly the same value as that from the theoretical calculation in which the actual conductor loss of the electroplated gold electrode has been considered. This bandwidth is limited by the relatively low conductivity of the poorly electroplated gold electrode and can be enhanced by improving the electroplating quality. The measured return loss is well below -20 dB. This low return loss is mainly due to the excellent impedance matching, as well as the smooth electric-field transformation in the CPW–microstrip–CPW transition. It can be noticed that this value is still higher than the theoretical result (-27 dB), probably due to the fabrication imperfection. The periodic ripples in the return loss curve are attributed to the RF Fabry–Perot effect. It is
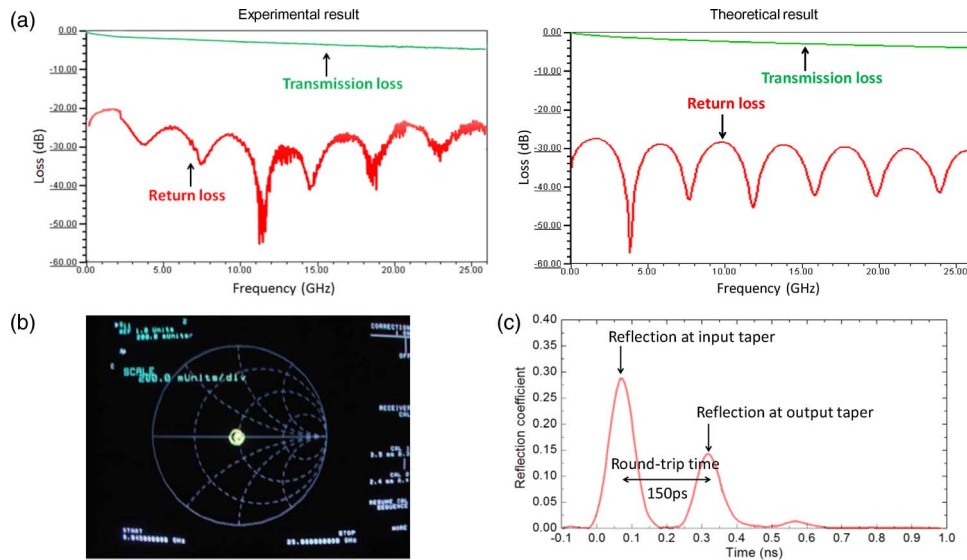
Fig. 9. (a) The measured transmission loss and return loss of the fabricated traveling-wave electrode over the frequency range 1–26 GHz (left side), almost matching the theoretical calculations (right side). (b) The measured characteristic impedance of the fabricated traveling-wave electrode is well centered at 50 Ω on Smith Chart, indicating impedance matching. (c) The time domain measurement of the reflection loss, for the demonstration of velocity matching.
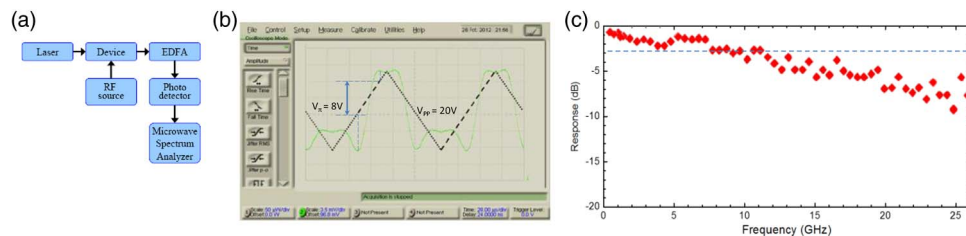

Fig. 10. (a) The schematic of testing system for small signal optical modulation measurement. (b) Transfer function of over-modulation with $V_{pp} = 40$ V at 10 kHz (wavelength = 1550 nm). The switching voltage is measured to be 16.5 V. (c) The frequency response of the small signal modulation measured at 4% modulation depth. The 3-dB bandwidth is measured to be 10 GHz.

shown in Fig. 9(b) that the characteristic impedance is well centered at 50 Ω on the Smith chart, indicating impedance matching. The velocity matching between microwaves and optical waves is evaluated by the time domain measurement of the return loss, as shown in Fig. 9(c). The effective relative dielectric constant of the microstrip line is measured to be 2.76, and the resulting index mismatch between microwaves and optical waves is 0.06. Then, the bandwidth–length product due to this velocity mismatch can be calculated by (3) to be 302 GHz · cm, so the modulation frequency limit corresponding to 2-cm interaction length would be 151 GHz, which matches the theoretical calculation result [153 GHz from Fig. 5(c)] pretty well.

4.2. Small Signal Optical Modulation Measurement

The frequency response of the device is evaluated by the small signal optical modulation measured at 4% modulation depth. The testing system is shown in Fig. 10(a). TM-polarized light with 1550-nm wavelength from a tunable laser (Santec ML-200, Santec Corporation) is butt-coupled into the waveguide through a single-mode fiber. The measured optical insertion loss is 16 dB, which includes propagation loss of 9 dB (absorption loss of 2 dB/cm for AJ-CKL1 times the total device length of 3 cm, scattering loss of 1 dB/cm times 3 cm), coupling loss of 6 dB (3 dB/fact times 2 facets),
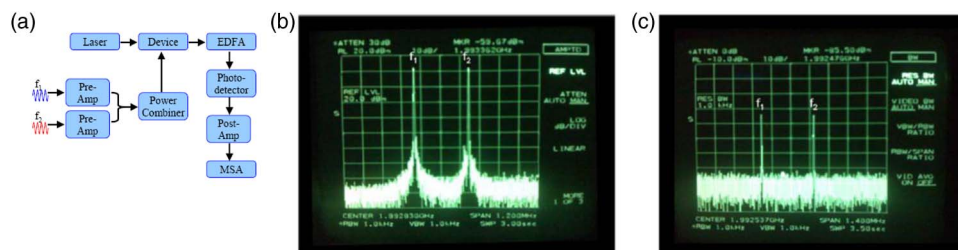
Fig. 11. (a) The schematic of system for two-tone test. (b) Input two-tone signals (f_1 and f_2) centered at 1.9928 GHz with 330 kHz tone interval. (c) Measured output fundamental signals.

and 1-dB loss from the MMI splitter. This relatively high loss is attributed to the roughness of the 3-cm-long waveguide sidewalls generated in RIE process and the roughness of input and output waveguide facets. To measure the switching voltage (V_π), a testing RF signal with $V_{pp} = 20$ V at 10 kHz is used. The transfer function of an overmodulation test is shown in Fig. 10(b). The switching voltage is measured to be 8 V at 10 kHz, which is a little high probably due to the low poling efficiency of EO polymer and electrode loss. For the small signal optical modulation, RF signal from HP 83651B is fed into the traveling-wave electrode through a GSG microprobe. The modulated optical signal is boosted by an erbium-doped fiber amplifier (Intelligain, Bay Spec Inc.), converted to electrical signal by a photodiode (DSC-R409, Discovery Semiconductors Inc.), and then measured by a microwave spectrum analyzer (HP 8560E). The frequency response measured at 4% modulation depth is presented in Fig. 10(c), from which the 3-dB bandwidth of the device can be found to be 10 GHz. This bandwidth is mainly limited by conductor loss of the traveling-wave electrode.

4.3. Linearity Evaluation

A two-tone test is performed to evaluate the linearity of the device. The testing system is illustrated in Fig. 11(a). HP 8620C sweep oscillator is used as the second RF source for the two-tone input signals. Agilent 83020A and HP8449B are used as pre- and post-RF amplifiers, respectively. The two input RF signals are combined by a coaxial two-way RF power combiner (RFLT2W1G04G, RF-Lambda). New Focus model-1014 is used for optical-to-electrical conversion of the modulated signal. The two-tone input signals and the resulting output signals are shown in Fig. 11(b) and (c), respectively. IMD3 signals, which are supposed to appear at one-tone interval away from the fundamental signals if present, are not observed in Fig. 11(c). A possible reason is that the IMD3 signals are well suppressed and buried under the noise floor at this modulation depth. The power level of the two-tone input signals is 12 dBm, as shown in Fig. 11(b), which is the maximum level available in our two-tone test setup, and this power level translates into the modulation depth of 15%. The simulation result in [28] predicts the IMD3 suppression at 15% modulation depth to be 74 dB, and the corresponding experimental result in [10] is 69 dB, which is a reasonable value considering the fabrication and measurement errors. Neglecting the performance degradation due to microwave loss and velocity mismatch, IMD3 signals would be 30 dB below the noise floor in Fig. 11(b) at 1-kHz bandwidth resolution.

Since the IMD3 suppression of the fabricated device is out of the measurable range in our two-tone test setup, SFDR is evaluated through an indirect method. It is known that, with the same modulation depth for both tones, IMD3 is three times or 9.54 dB higher than the third-harmonic distortion [58]. A monotone test is done under the same conditions as the two-tone test. The power level of monotone input signal is extended up to 29 dBm by combining the RF source (HP 83651B) with the preamplifier (Agilent 83020A). It is found that the third-harmonic distortion of our device comes in the detectable range at the monotone input signal level above 20 dBm. The IMD3 signals are obtained by adding 9.54 dB to the measured third-harmonic distortion signals. The SFDR is measured by extrapolating the IMD3 plot to find an intercept point with the noise floor and then measuring the difference with the extrapolated fundamental signal as illustrated in Fig. 12(a). Considering the relative intensity noise (RIN) of the distributed feedback (DFB) laser and the shot noise
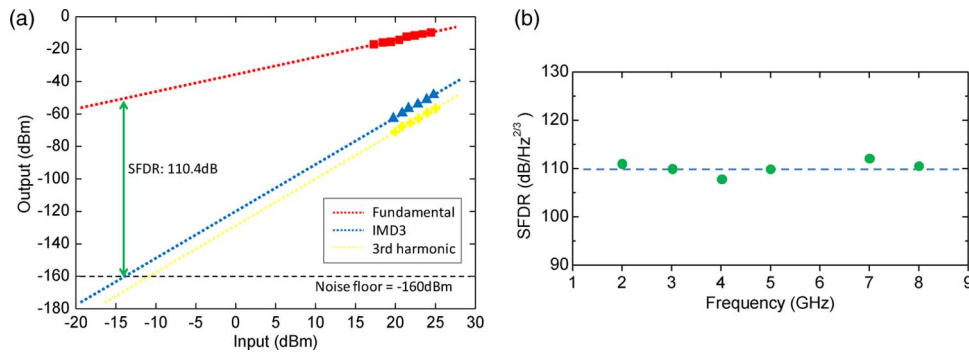
Fig. 12. (a) The plot of fundamental and third-order intermodulation distortion signals measured at 8 GHz. (b) Spurious-free dynamic range measured at 2–8 GHz.

of the photodiode, it is very difficult to achieve a noise floor below -145 dBm in real analog optical links [28]. However, laboratory test results in most literatures are frequently presented assuming the noise floor at -160 dBm considering the typical fiber-optic link parameters [2], [59], [60]. Using -160 dBm as noise floor, our measured SFDR is within 110 ± 3 dB/Hz$^{2/3}$ over the modulation frequency range of 2–8 GHz, as shown in Fig. 12(b). The low end frequency is determined by the operation range (2–26.5 GHz) of the preamplifier (Agilent 83020A), and the high end is limited to 8 GHz because the third harmonic of the modulation frequency above 8 GHz goes beyond the scope (~ 26.5 GHz) of the microwave spectrum analyzer. The SFDR at 6 GHz is missing due to the irregular gain of the postamplifier at 18 GHz. As a comparison, Schaffner et $al.$ reported the SFDR of 109.6 dB/Hz$^{2/3}$ at 1 GHz with a LiNibO$_3$ directional coupler modulator, which is linearized by adding passive bias sections [1]. In their measurement, however, the noise floor was set at -171 dBm, which offers 7.3-dB extra dynamic range compared with the noise floor at -160 dBm. Hung et $al.$ achieved even higher SFDR of 115.5 dB/Hz$^{2/3}$ at 3 GHz with a linearized polymeric directional coupler modulator by subtracting the distortions of the measurement system [60]. Here, our SFDR of 110 ± 3 dB/Hz$^{2/3}$ includes the distortions from the entire measurement system as well as the device. To the best of our knowledge, such high linearity is first measured at a frequency up to 8 GHz.

5. Conclusion

We have demonstrated a linearized traveling-wave MMI-fed directional coupler modulator based on EO polymer. Domain-inversion poling is applied to implement the $\Delta \beta$-reversal technique. The traveling-wave electrode has been evaluated to be functional up to 151 GHz for our device design due to the excellent velocity matching between microwaves and optical waves. The SFDR of 110 ± 3 dB/Hz$^{2/3}$ has been achieved over the modulation frequency of 2–8 GHz. The measured 3-dB bandwidth of the device is 10 GHz, which is mainly limited by conductor loss and needs further improvement for practical applications. The optical loss still needs to be further suppressed for application, and this will be improved in our future work by choosing low loss sol-gel passive materials and by using wet etching method for waveguide fabrication [61].

References

[1] J. H. Schaffner, J. F. Lam, C. J. Gaeta, G. L. Tangonan, R. L. Joyce, M. L. Farwell, and W. S. C. Chang, "Spur-free dynamic range measurements of a fiber optic link with traveling wave linearized directional coupler modulators," $IEEE$ $Photon.$ $Technol.$ $Lett.$, vol. 6, no. 2, pp. 273–275, Feb. 1994.
[2] R. B. Childs and V. A. O'Byrne, "Predistortion linearization of directly modulated DFB lasers and external modulators for AM video transmission," presented at the Proc. Optical Fiber Communication Conf., San Francisco, CA, 1990, Paper WH6.
[3] R. M. D. E. Ridder and S. Korotky, "Feedforward compensation of integrated optic modulator distortion," presented at the Proc. Optical Fiber Communication Conf., San Francisco, CA, 1990, Paper WH6.
[4] L. M. Johnson and H. Roussell, "Reduction intermodulation distortion in interferometric optical modulators," $Opt.$ $Lett.$, vol. 13, no. 10, pp. 928–930, Oct. 1988.

 [5] S. K. Korotky and R. De Ridder, "Dual parallel modulation schemes for low-distortion analog optical transmission," *IEEE J. Sel. Areas Commun.*, vol. 8, no. 7, pp. 1377–1381, Sep. 1990.

 [6] M. L. Farwell, Z. Q. Lin, E. Wooten, and W. Chang, "An electrooptic intensity modulator with improved linearity," *IEEE Photon. Technol. Lett.*, vol. 3, no. 9, pp. 792–795, Sep. 1991.

 [7] S. Thaniyavarn, "Modified 1 × 2 directional coupler waveguide modulator," *Electron. Lett.*, vol. 22, no. 18, pp. 941–942, Aug. 1986.

 [8] H. Kogelnik and R. V. Schmidt, "Switched directional couplers with alternating $\Delta\beta$," *IEEE J. Quantum Electron.*, vol. 12, no. 7, pp. 396–401, Jul. 1976.

 [9] R. F. Tavlykaev and R. V. Ramaswamy, "Highly linear Y-fed directional coupler modulator with low intermodulation distortion," *J. Lightw. Technol.*, vol. 17, no. 2, pp. 282–291, Feb. 1999.

[10] B. Lee, C. Y. Lin, A. X. Wang, R. Dinu, and R. T. Chen, "Linearized electro-optic modulators based on a two-section Y-fed directional coupler," *Appl. Opt.*, vol. 49, no. 33, pp. 6485–6488, Nov. 2010.

[11] M. Izutsu, Y. Yamane, and T. Sueta, "Broad-band traveling-wave modulator using a LiNbO3 optical waveguide," *IEEE J. Quantum Electron.*, vol. 13, no. 4, pp. 287–290, Apr. 1977.

[12] M. Izutsu, T. Itoh, and T. Sueta, "10 GHz bandwidth traveling-wave LiNbO3 optical waveguide modulator," *IEEE J. Quantum Electron.*, vol. 14, no. 6, pp. 394–395, Jun. 1978.

[13] C. Teng, "Traveling-wave polymeric optical intensity modulator with more than 40 GHz of 3-dB electrical bandwidth," *Appl. Phys. Lett.*, vol. 60, no. 13, pp. 1538–1540, Mar. 1992.

[14] D. Chen, H. R. Fetterman, A. Chen, W. H. Steier, L. R. Dalton, W. Wang, and Y. Shi, "Demonstration of 110 GHz electro-optic polymer modulators," *Appl. Phys. Lett.*, vol. 70, no. 25, pp. 3335–3337, Jun. 1997.

[15] M. Lee, H. E. Katz, C. Erben, D. M. Gill, P. Gopalan, J. D. Heber, and D. J. McGee, "Broadband modulation of light by using an electro-optic polymer," *Science*, vol. 298, no. 5597, pp. 1401–1403, Nov. 2002.

[16] L. R. Dalton, A. W. Harper, B. Wu, R. Ghosn, J. Laquindanum, Z. Liang, A. Hubbel, and C. Xu, "Polymeric electro-optic modulators: Materials synthesis and processing," *Adv. Mater.*, vol. 7, no. 6, pp. 519–540, Jun. 1995.

[17] H. Ma, A. K. Y. Jen, and L. R. Dalton, "Polymer-based optical waveguides: Materials, processing, and devices," *Adv. Mater.*, vol. 14, no. 19, pp. 1339–1365, Oct. 2002.

[18] M. C. Oh, H. Zhang, C. Zhang, H. Erlig, Y. Chang, B. Tsap, D. Chang, A. Szep, W. H. Steier, and H. R. Fetterman, "Recent advances in electrooptic polymer modulators incorporating highly nonlinear chromophore," *IEEE J. Sel. Topics Quantum Electron.*, vol. 7, no. 5, pp. 826–835, Sep./Oct. 2001.

[19] Y. Shi, C. Zhang, H. Zhang, J. H. Bechtel, L. R. Dalton, B. H. Robinson, and W. H. Steier, "Low (sub-1-volt) halfwave voltage polymeric electro-optic modulators achieved by controlling chromophore shape," *Science*, vol. 288, no. 5463, pp. 119–122, Apr. 2000.

[20] Y. Enami, C. Derose, D. Mathine, C. Loychik, C. Greenlee, R. Norwood, T. Kim, J. Luo, Y. Tian, and A. K. Y. Jen, "Hybrid polymer/sol–gel waveguide modulators with exceptionally large electro–optic coefficients," *Nat. Photon.*, vol. 1, no. 3, pp. 180–185, 2007.

[21] Y. Enami, D. Mathine, C. DeRose, R. Norwood, J. Luo, A. K. Y. Jen, and N. Peyghambarian, "Hybrid cross-linkable polymer/sol–gel waveguide modulators with 0.65 V half wave voltage at 1550 nm," *Appl. Phys. Lett.*, vol. 91, no. 9, pp. 093505-1–093505-3, Aug. 2007.

[22] J. Luo, S. Huang, Y. J. Cheng, T. D. Kim, Z. Shi, X. H. Zhou, and K. Y. J. Alex, "Phenyltetraene-based nonlinear optical chromophores with enhanced chemical stability and electrooptic activity," *Organ. Lett.*, vol. 9, no. 22, pp. 4471–4474, Oct. 2007.

[23] T. Baehr-Jones, M. Hochberg, G. Wang, R. Lawson, Y. Liao, P. Sullivan, L. Dalton, A. K. Y. Jen, and A. Scherer, "Optical modulation and detection in slotted silicon waveguides," *Opt. Exp.*, vol. 13, no. 14, pp. 5216–5226, Jul. 2005.

[24] J. H. Wülbern, J. Hampe, A. Petrov, M. Eich, J. Luo, A. K. Y. Jen, A. Di Falco, T. F. Krauss, and J. Bruns, "Electro-optic modulation in slotted resonant photonic crystal heterostructures," *Appl. Phys. Lett.*, vol. 94, no. 24, pp. 241107-1–241107-3, Jun. 2009.

[25] X. Wang, C. Y. Lin, S. Chakravarty, J. Luo, A. K. Y. Jen, and R. T. Chen, "Effective in-device r_{33} of 735 pm/V on electro-optic polymer infiltrated silicon photonic crystal slot waveguides," *Opt. Lett.*, vol. 36, no. 6, pp. 882–884, Mar. 2011.

[26] A. C. G. Nutt, V. Gopalan, and M. C. Gupta, "Domain inversion in LiNbO3 using direct electron-beam writing," *Appl. Phys. Lett.*, vol. 60, no. 23, pp. 2828–2830, Jun. 1992.

[27] D. Jin, H. Chen, A. Barklund, J. Mallari, G. Yu, E. Miller, and R. Dinu, "EO polymer modulators reliability study," in *Proc. SPIE*, 2010, vol. 7599, pp. 75990H-1–75990H-8.

[28] X. Wang, B. S. Lee, C. Y. Lin, D. An, and R. T. Chen, "Electroptic polymer linear modulators based on multiple-domain Y-fed directional coupler," *J. Lightw. Technol.*, vol. 28, no. 11, pp. 1670–1676, Jun. 2010.

[29] B. Lee, C. Lin, X. Wang, R. T. Chen, J. Luo, and A. K. Y. Jen, "Bias-free electro-optic polymer-based two-section Y-branch waveguide modulator with 22 dB linearity enhancement," *Opt. Lett.*, vol. 34, no. 21, pp. 3277–3279, Nov. 2009.

[30] FIMMWAVE Simulation Software. [Online]. Available: http://www.photond.com/products/fimmwave.htm

[31] FIMMPROP Simulation Software. [Online]. Available: http://www.photond.com/products/fimmprop.htm

[32] G. T. Reed, *Silicon Photonics: The State of the Art.*   Chichester, U.K.: Wiley, 2008.

[33] COMSOL Multiphysics Simulation Software. [Online]. Available: http://www.comsol.com

[34] R. G. Hunsperger, A. Yariv, and A. Lee, "Parallel end-butt coupling for optical integrated circuits," *Appl. Opt.*, vol. 16, no. 4, pp. 1026–1032, Apr. 1977.

[35] M. Sanghadasa, P. R. Ashley, E. L. Webster, C. Cocke, G. A. Lindsay, and A. J. Guenthner, "A simplified technique for efficient fiber-polymer-waveguide power coupling using a customized cladding with tunable index of refraction," *J. Lightw. Technol.*, vol. 24, no. 10, pp. 3816–3823, Oct. 2006.

[36] K. Geary, S. K. Kim, B. J. Seo, Y. C. Hung, W. Yuan, and H. R. Fetterman, "Photobleached refractive index tapers in electrooptic polymer rib waveguides," *IEEE Photon. Technol. Lett.*, vol. 18, no. 1, pp. 64–66, Jan. 2006.

[37] I. E. Day, I. Evans, A. Knights, F. Hopper, S. Roberts, J. Johnston, S. Day, J. Luff, H. K. Tsang, and M. Asghari, "Tapered silicon waveguides for low insertion loss highly-efficient high-speed electronic variable optical attenuators," in *Proc. Opt. Fiber Commun. Conf.*, 2003, pp. 249–251.

[38] Rsoft Simulation Software. [Online]. Available: http://www.rsoftdesign.com/
[39] W. S. Chang, *RF Photonic Technology in Optical Fiber Links*. Cambridge, U.K.: Cambridge Univ. Press, 2002.
[40] D. Chen, Q. Wang, and Z. Shen, "A broadband microstrip-to-CPW transition," in *Proc. APMC*, 2005, p. 4.
[41] Y. G. Kim, K. W. Kim, and Y. K. Cho, "An ultra-wideband Microstrip-to-CPW transition," in *Proc. IEEE MTT-S*, Atlanta, GA, 2008, pp. 1079–1082.
[42] E. Yamashita, "Variational method for the analysis of microstrip-like transmission lines," *IEEE Trans. Microw. Theory Tech.*, vol. 16, no. 8, pp. 529–535, Aug. 1968.
[43] ANSYS HFSS Simulation Software. [Online]. Available: http://www.ansys.com/
[44] A. Chen and E. Murphy, *Broadband Optical Modulators: Science, Technology, and Applications*. Boca Raton, FL: CRC Press, 2011.
[45] R. C. Alferness, "Waveguide electrooptic modulators," *IEEE Trans. Microw. Theory Tech.*, vol. MTT-30, no. 8, pp. 1121–1137, Aug. 1982.
[46] D. M. Burland, R. D. Miller, and C. A. Walsh, "Second-order nonlinearity in poled-polymer systems," *Chem. Rev.*, vol. 94, no. 1, pp. 31–75, Jan. 1994.
[47] L. R. Dalton, P. A. Sullivan, and D. H. Bale, "Electric field poled organic electro-optic materials: State of the art and future prospects," *Chem. Rev.*, vol. 110, no. 1, pp. 25–55, Jan. 2009.
[48] M. A. Mortazavi, A. Knoesen, S. T. Kowel, B. G. Higgins, and A. Dienes, "Second-harmonic generation and absorption studies of polymer—Dye films oriented by corona-onset poling at elevated temperatures," *J. Opt. Soc. Amer. A, Opt. Phys.*, vol. 6, no. 4, pp. 733–741, Apr. 1989.
[49] H. Tang, J. M. Taboada, G. Cao, L. Li, and R. T. Chen, "Enhanced electro-optic coefficient of nonlinear optical polymer using liquid contact poling," *Appl. Phys. Lett.*, vol. 70, no. 5, pp. 538–540, Feb. 1997.
[50] Z. Z. Yue, D. An, R. T. Chen, and S. Tang, "1000 V/μm pulsed poling technique for photolime-gel electro-optic polymer with room-temperature repoling feature," *Appl. Phys. Lett.*, vol. 72, no. 26, pp. 3420–3421, Jun. 1998.
[51] S. Huang, T. D. Kim, J. Luo, S. K. Hau, Z. Shi, X. H. Zhou, H. L. Yip, and A. K. Y. Jen, "Highly efficient electro-optic polymers through improved poling using a thin TiO-modified transparent electrode," *Appl. Phys. Lett.*, vol. 96, no. 24, pp. 243311-1–243311-3, Jun. 2010.
[52] S. Huang, J. Luo, H. L. Yip, A. Ayazi, X. H. Zhou, M. Gould, A. Chen, T. Baehr-Jones, M. Hochberg, and A. K. Y. Jen, "Electro-optical materials: Efficient poling of electro-optic polymers in thin films and silicon slot waveguides by detachable pyroelectric crystals (Adv. Mater. 10/2012)," *Adv. Mater.*, vol. 24, no. 10, p. OP1, Mar. 2012.
[53] R. Blum, M. Sprave, J. Sablotny, and M. Eich, "High-electric-field poling of nonlinear optical polymers," *J. Opt. Soc. Amer. B, Opt. Phys.*, vol. 15, no. 1, pp. 318–328, Jan. 1998.
[54] T. A. Tumolillo, Jr, and P. R. Ashley, "A novel pulse-poling technique for EO polymer waveguide devices using device electrode poling," *IEEE Photon. Technol. Lett.*, vol. 4, no. 2, pp. 142–145, Feb. 1992.
[55] V. Taggi, F. Michelotti, M. Bertolotti, G. Petrocco, V. Foglietti, A. Donval, E. Toussaere, and J. Zyss, "Domain inversion by pulse poling in polymer films," *Appl. Phys. Lett.*, vol. 72, no. 22, pp. 2794–2796, Jun. 1998.
[56] J. Baker-Jarvis, M. D. Janezic, B. Riddle, C. L. Holloway, and N. Paulter, "Dielectric and conductor-loss characterization and measurements on electronic packaging materials," NIST, Gaithersburg, MD, Nist Tech. Note 1520, 2001.
[57] G. K. Gopalakrishnan, W. K. Burns, R. W. McElhanon, C. H. Bulmer, and A. S. Greenblatt, "Performance and modeling of broadband LiNbO3 traveling wave optical intensity modulators," *J. Lightw. Technol.*, vol. 12, no. 10, pp. 1807–1819, Oct. 1994.
[58] P. L. Liu, B. Li, and Y. Trisno, "In search of a linear electrooptic amplitude modulator," *IEEE Photon. Technol. Lett.*, vol. 3, no. 2, pp. 144–146, Feb. 1991.
[59] W. B. Bridges and J. H. Schaffner, "Distortion in linearized electrooptic modulators," *IEEE Trans. Microw. Theory Tech.*, vol. 43, no. 9, pp. 2184–2197, Sep. 1995.
[60] Y. C. Hung, S. K. Kim, H. Fetterman, J. Luo, and A. K. Y. Jen, "Experimental demonstration of a linearized polymeric directional coupler modulator," *IEEE Photon. Technol. Lett.*, vol. 19, no. 21, pp. 1762–1764, Nov. 2007.
[61] C. T. DeRose, R. Himmelhuber, D. Mathine, R. Norwood, J. Luo, A. K. Y. Jen, and N. Peyghambarian, "High Δn strip-loaded electro-optic polymer waveguide modulator with low insertion loss," *Opt. Exp.*, vol. 17, no. 5, pp. 3316–3321, Mar. 2009.